Chern numbers of topological phonon band crossing determined with inelastic neutron scattering

Zhendong Jin,[1,*] Biaoyan Hu,[1,*] Yiran Liu [ORCID],[1,*] Yangmu Li [ORCID],[2,3,4] Tiantian Zhang,[2] Kazuki Iida,[5] Kazuya Kamazawa,[5]
A. I. Kolesnikov [ORCID],[6] M. B. Stone [ORCID],[6] Xiangyu Zhang,[7] Haiyang Chen,[7] Yandong Wang,[7] I. A. Zaliznyak [ORCID],[3]
J. M. Tranquada [ORCID],[3] Chen Fang,[2,†] and Yuan Li [ORCID][1,8,‡]

[1]*International Center for Quantum Materials, School of Physics, Peking University, Beijing 100871, China*
[2]*Beijing National Laboratory for Condensed Matter Physics, and Institute of Physics, Chinese Academy of Sciences, Beijing 100190, China*
[3]*Condensed Matter Physics and Materials Science Division, Brookhaven National Laboratory, Upton, New York 11973, USA*
[4]*School of Physical Sciences, University of Chinese Academy of Sciences, Beijing 100049, China*
[5]*Neutron Science and Technology Centre,*
Comprehensive Research Organisation for Science and Society (CROSS), Tokai, Ibaraki 319-1106, Japan
[6]*Neutron Scattering Division, Oak Ridge National Laboratory, Oak Ridge, Tennessee 37831, USA*
[7]*State Key Laboratory for Advance Metals and Materials, University of Science and Technology Beijing, Beijing 10083, China*
[8]*Collaborative Innovation Center of Quantum Matter, Beijing 100871, China*

Topological invariants in the band structure, such as Chern numbers, are important for the understanding and classification of the topological properties of matter and dictate the occurrence of exotic behaviors, yet their direct spectroscopic determination has been largely limited to electronic bands. Here, we use inelastic neutron scattering in conjunction with *ab initio* calculations to identify a variety of topological phonon band crossings in MnSi and CoSi single crystals. We find a distinct relation between the Chern numbers of a band-crossing node and the scattering intensity modulation in momentum space around the node. Given sufficiently high resolution, our method can be used to determine arbitrarily large Chern numbers of topological phonon band-crossing nodes.

I. INTRODUCTION

Ever since the discovery of topological quantum numbers in quantum Hall states [1,2], the concept of band topology has shed light on the exploration and classification of crystalline materials [3–7]. Topological insulators, semimetals, and superconductors are extensively studied, both as novel phases of matter and for their potential applications. Unlike conventional phases of matter described by symmetry in the Landau paradigm, topological phases are classified by topological invariants, which do not change under adiabatic deformations of the band structure.

An important topological invariant is called the Chern number, which is associated with a mapping from a two-dimensional (2D) closed surface in reciprocal space to the Hilbert space of Bloch states. The Chern number characterizes the topological structure of such mapping and has observable consequences. In the gapped energy spectrum of 2D quantum Hall systems, nonzero Chern numbers correspond to the number of edge states, which lead to the quantization of the Hall conductance [3,8]. In three-dimensional (3D) Weyl semimetals, Weyl nodes act as monopoles of Berry flux and have nonzero Chern numbers (defined by the mapping from their enclosing surface in momentum space to the Hilbert space), which determine the number of

Fermi-arc surface states [9–11] and the quantized magnitude of circular photogalvanic effect [12,13]. As the essence of topological band theory is independent of the statistics of the constituent quasiparticles, much effort has been devoted to the search for similar topological bands in bosonic systems. In artificial structures, topological photonic and acoustic bands and their corresponding surface states have been predicted and observed by various spectroscopy methods [14–18]. The discrete transport of such edge modes has also been confirmed in photonic crystals, as the jump in microwave transmission coefficient matches the number of edge modes defined by the Chern numbers [19]. In natural crystals, many predictions have been made on such distinguished surface states from bulk topological phonons [20–26] and magnons [27–31], but they have not been observed since common probes cannot single out surface states from the bulk ones. Besides the surface states, the physical consequences of topological bosons are rather limited compared to the electronic case, as the phonons and magnons do not carry charges and there is no Fermi surface. Thermal measurements are still possible, such as anomalous thermal Hall effects arising from nonzero Berry curvatures of topological phonons [32] and magnons [27,33]. Another possibility is gauge-field-induced chiral phonon mode with Aharonov-Bohm-type effects in nanomechanical systems [34]. Yet these are all subtle effects that need demanding measurements. Given that accessible observables of bosonic band topology are still very limited to date, practical methods for determining Chern numbers in phonon and magnon bands are desired.

---

*These authors contributed equally to this work.
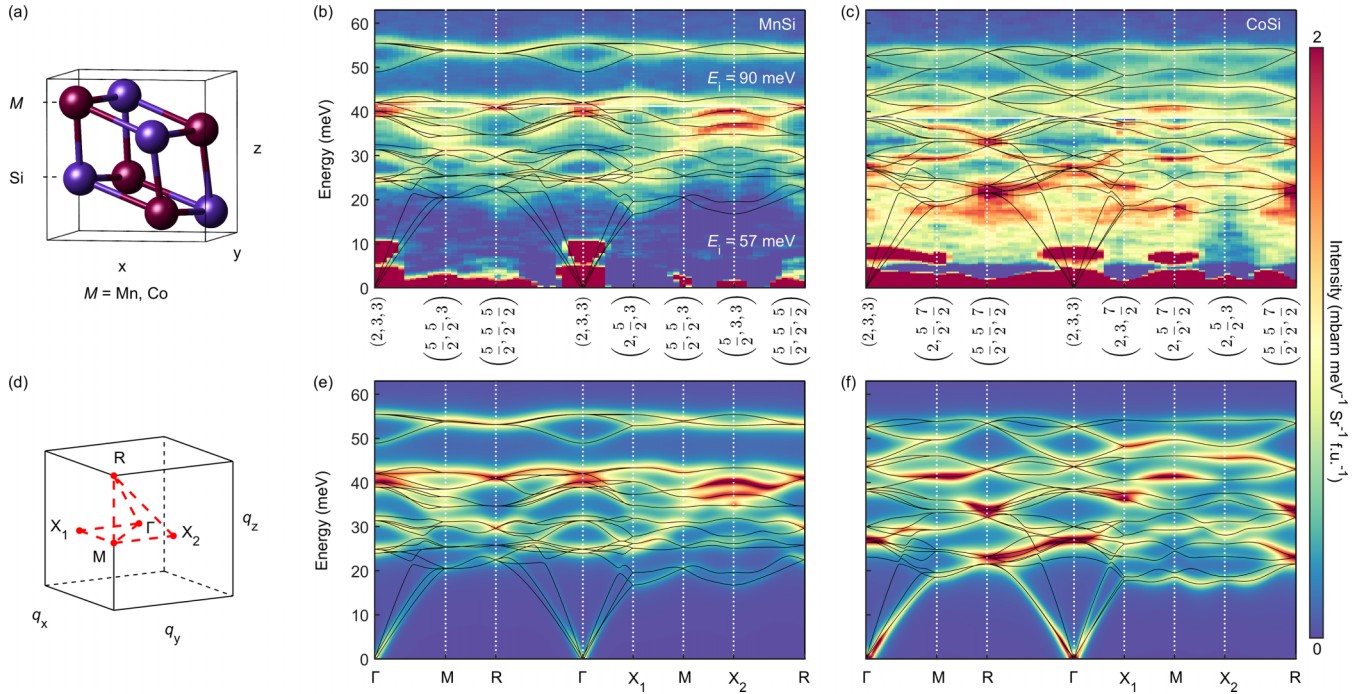†cfang@iphy.ac.cn
‡yuan.li@pku.edu.cn

FIG. 1. (a) Cubic unit cell of MSi (M = Mn, Co). (b) and (c) Representative INS intensities of MnSi and CoSi, respectively, along a high-symmetry momentum trajectory, measured at T = 40 K. Data measured with E_i = 57 meV and 90 meV are combined after proper intensity normalization. (d) The Brillouin zone (BZ), with the momentum trajectory marked in red. (e) and (f) $\mathcal{S}(\mathbf{Q}, \omega)$ calculated from the fitted-force-constant model along the same trajectories as in (b) and (c). Solid lines in (b), (c), (e), and (f) indicate the calculated phonon dispersions.

It is experimentally possible to determine Chern numbers in phonon and magnon bands, if one can measure the topological structure of wave functions, i.e., eigenvectors in momentum space. Scattering methods such as inelastic neutron scattering (INS) and x-ray scattering are suitable for this purpose, because their dynamical structure factor $\mathcal{S}(\mathbf{Q}, \omega)$ is determined by the excitations' eigenvectors [35,36]. As the eigenvectors vary strongly in the vicinity of Weyl and Dirac points, the observed intensities are expected to undergo strong and distinct modulations, which can reflect the topological structure of the excitation spectrum. Such modulations have been recently reported in several topological magnon systems around Dirac points [37,38] and nodal lines [39,40].

Here, we report an INS study of MSi (M = Co, Mn) single crystals, which host multiple types of topological phonon band crossing nodes [22,23,41]. Except for their linear dispersions, potential physical consequences of such topological phonons, including the surface modes [22] and the possible anomalous thermal Hall effect [32], remain largely unexplored. By comparing the observed INS intensities with our fitted model based on density functional perturbation theory (DFPT) calculations, we verify the theoretically predicted coexistence of twofold quadruple Weyl points, threefold spin-1 Weyl points, and fourfold charge-2 Dirac points in MSi. We further explore the spectroscopic signatures of topological structures near the topological band crossing points and show, theoretically and in some cases with comparison to the experimental data, that the number of intensity extrema on a momentum sphere enclosing the band-crossing node equals the Chern number of the node. Our result demonstrates the capability of INS for direct Chern-number determination.

This paper is organized as follows: In Sec. II, we describe the INS experiment and the fitted-force-constant model based on DFPT. In Sec. III, we show phonon dispersions, both in a global view and close to topological band crossing nodes. In Sec. IV, we discuss INS spectroscopic features near the band-crossing nodes and investigate their relation with the Chern numbers. In Sec. V, we make a brief discussion and a summary.

II. EXPERIMENT AND CALCULATION METHODS

A. INS experiment

High-quality single crystals of MnSi and CoSi were grown by a traveling floating zone method. The INS experiments were performed on the 4SEASONS spectrometer at MLF, J-PARC, Japan and the SEQUOIA spectrometer at SNS, ORNL, USA [42,43]. A total of 33 (28) grams of MnSi (CoSi) twin-free single crystals with a mosaic spread of $\lesssim$ 1.3° full-width at half-maximum (FWHM) were used for the experiments (Fig. S1 [44,45]). The INS data shown in this paper were collected with incident neutron energies E_i = 57 and 90 meV at a fixed temperature of T = 40 K, and analyzed with the UTSUSEMI and HORACE software [46,47]. As MnSi and CoSi share the $B20$-type structure belonging to the noncentrosymmetric space group $P2_13$ [Fig. 1(a)], data from equivalent momenta have been symmetrized and averaged accordingly in order to improve counting statistics. Intensities are presented in absolute scattering cross sections by using the incoherent elastic scattering of the sample for normalization (Fig. S2, [44,48]). To best visualize the phonon cross sections, we present coherent scattering signals from the sample only,

whereas intensities arising from incoherent scattering of the sample and from the aluminum sample holders have been subtracted as background (see more details in Sec. III in Ref. [44]).

B. Fitted-force-constant model

The phonon force constant matrices of CoSi and MnSi were calculated with the Vienna *ab initio* simulation package (VASP) [49–53] using the DFPT method. The calculations were done with the Perdew-Burke-Ernzerhof (PBE)-type exchange-correlation functional, under the generalized gradient approximation (GGA) [54]. The kinetic energy cutoff was set to 400 eV. Integrations over the Brillouin zone were performed with Monkhorst-Pack $\mathbf{Q}$-point grids (equivalent to $12 \times 12 \times 12$ grid for CoSi and $15 \times 15 \times 15$ grid for MnSi). Lattice constants and atomic positions were relaxed until residual forces drop below 0.001 eV/Å. The relaxed lattice constants were 4.35 Å for CoSi and 4.42 Å for MnSi, which are slightly smaller than our experimental values, 4.43 ± 0.02 Å for CoSi and 4.56 ± 0.01 Å for MnSi. After obtaining the band dispersion $\omega(\mathbf{Q})$, the coherent dynamical structure factors $\mathcal{S}_{\mathrm{coh}}^{(s)}(\mathbf{Q}, \omega)$ for all vibration modes (s) were written as [35,36,55]

$$\mathcal{S}_{\mathrm{coh}}^{(s)}(\mathbf{Q}, \omega) = \frac{(2\pi)^3}{V_0} \sum_{\mathbf{G},\mathbf{q}} \frac{|F_{\mathrm{coh}}^{(s)}(\mathbf{Q})|^2}{2\omega^{(s)}(\mathbf{q})}$$
$$\times \delta(\mathbf{Q} - \mathbf{q} - \mathbf{G})\delta(\omega - \omega^{(s)}(\mathbf{q})),$$
$$F_{\mathrm{coh}}^{(s)}(\mathbf{Q}) = \sum_d \frac{b_{d,\mathrm{coh}}}{\sqrt{m_d}} \mathbf{Q} \cdot \boldsymbol{\xi}_d^{(s)}(\mathbf{q}) e^{i\mathbf{Q}\cdot\mathbf{r}_d}, \qquad (1)$$

where $\mathbf{Q} = \mathbf{q} + \mathbf{G}$ is the total momentum transfer with $\mathbf{G}$ being a reciprocal lattice vector, V_0 is the total volume, and m_d, $\mathbf{r}_d$, $b_{d,\mathrm{coh}}$, $\boldsymbol{\xi}_d^{(s)}(\mathbf{q})$ denote the mass, position, coherent scattering length, and eigenvector (see Eqs. 4.26 and 4.28 in Ref. [35]) of the dth atom in the unit cell.

Notably, the original DFPT results have deviations from the INS data, including a global rescaling in energies, slight distortions in the dispersions and scattering intensity (Fig. S4 [44]). Such deviations may stem from inaccuracy in the calculated crystal structure and force constants, or the correlation effects. A more accurate model description of the phonon bands can be obtained by performing parametric fits on the leading force constants while discarding the weaker interactions. The energy values of all phonon branches at high-symmetry points Γ, X, M, R are extracted from experiment spectra (Table S1 [44]) and used as fitting benchmarks. With about ten pairwise interactions, our model reproduces features in the experimental dispersions and intensities with satisfactory accuracy over many BZs (Fig. S4 [44]). All model calculation results in the main text are obtained with the optimized parameters listed in Table S2.

III. DISPERSION AND TOPOLOGICAL BAND CROSSING

To begin, we present in Figs. 1(b) and 1(c) representative INS spectra of MnSi and CoSi, respectively, along high-symmetry lines in the irreducible Brillouin zone (BZ) [Fig. 1(d)]. A wealth of phonon scattering signals are ob-

served. The strong contaminations below 10 meV originate from multiple scattering, since they only appear with specific incident neutron energy and geometry (see Fig. S5 [44]). Some residual aluminum scattering signals are also observed below 20 meV due to energy-dependent absorption [44]. They are more evident in the CoSi spectrum [Fig. 1(c)] than in MnSi because cobalt has a larger neutron absorption cross section [55]. Overall, the phonon INS signals compare favorably with our model calculations in Figs. 1(e) and 1(f). The model for MnSi is particularly satisfactory. This suggests that our fitted-force-constant model provides an adequate representation of the phonons.

Having established the model describing the phonon spectrum, we now zoom into the topological band crossings. We start from the Γ point at the BZ center. According to group theoretical analysis, phonons at the Γ point are irreducible representations of the tetrahedral $T(23)$ point group: $\Gamma = 2A + 2E + 6T$, where A, E, and T represent singly, doubly, and triply degenerated modes, respectively. Importantly, all threefold degenerate phonon band crossings at the Γ point form spin-1 Weyl points protected by the point-group symmetry [22], and all twofold degenerate phonons are quadruple Weyl points protected by the extra time-reversal symmetry $\mathcal{T}$ [41,56]. We have additionally verified the irreducible representations of the BZ-center phonons using polarized Raman spectroscopy (Fig. S6 [44]).

Based on the above information, we zoom into the spin-1 Weyl point at the highest energy (52.5 meV) in CoSi. The INS intensities along a R-Γ-R momentum trajectory are displayed in Fig. 2(a). This band crossing has relatively large dispersion velocities and is far away from other bands, yet, the fact that a total of three branches are involved in the crossing makes them challenging to resolve experimentally. By making energy line cuts and fitting the intensity profiles systematically [Fig. 2(b)], we find that the INS data do support a crossing of three bands. For comparison, fitting the spectra obtained symmetrically away from Γ with only two or fewer peaks does not yield a consistent description (Fig. S7(a) [44]). Similar energy line cuts along a M-Γ-M trajectory (Fig. S8) also agree with the existence of gapless three bands crossing at Γ point (52.5 meV). We thus conclude that the spin-1 Weyl point is present at Γ point in CoSi. In MnSi, however, all threefold degenerate modes at the Γ point are too close in energy to other phonon branches, precluding a similar analysis.

We next turn to the R point at the BZ corner, where all band crossings are fourfold degenerate charge-2 Dirac points protected by the crystallographic and $\mathcal{T}$ symmetries [22]. Here, a charge-2 Dirac point is the direct sum of two identical spin-1/2 Weyl points. Because the bands remain twofold degenerate along the $\overline{RX}$ and $\overline{RM}$ directions, we expect to observe only two linearly dispersing branches along these directions, which can be regarded as a key signature of the Dirac points. INS spectra consistent with such understanding are displayed near 41 meV for MnSi and 52 meV for CoSi in Figs. 2(c) and 2(e), respectively. The band crossings are also reproduced in our model calculations [Figs. 2(d) and 2(f)]. Energy cuts at a series of successive $\mathbf{Q}$ positions [Fig. 2(e)] further confirm the approximate linear band crossing [Fig. 2(g)], and a similar case for CoSi is displayed in Fig. S7(b) [44]. For MnSi, the fitted-force-constant model also
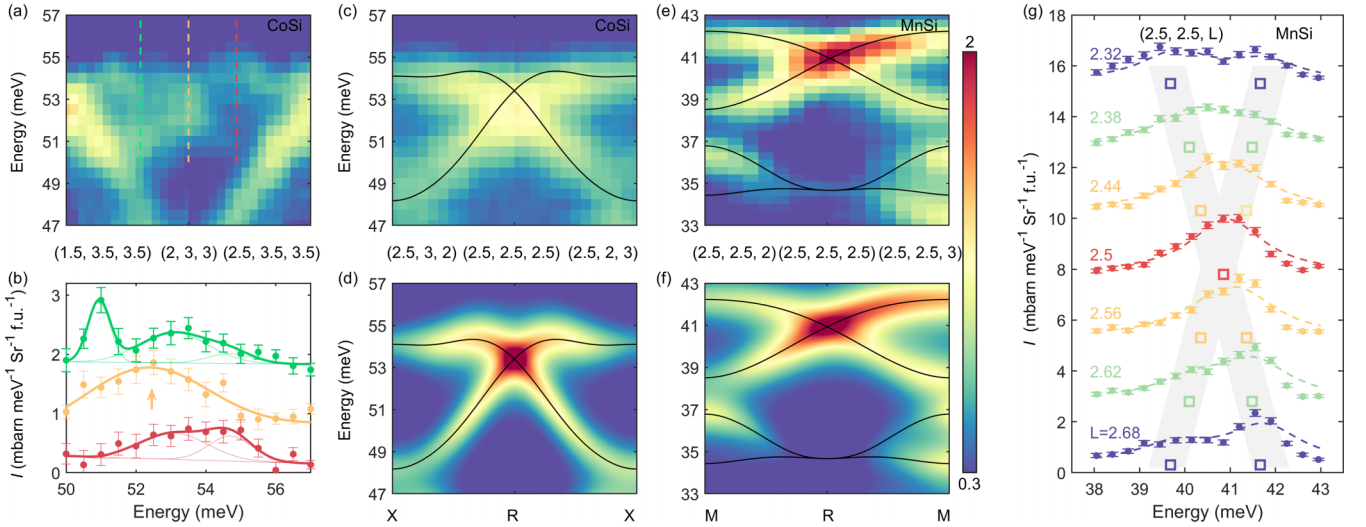
FIG. 2. (a) INS spectra near a spin-1 Weyl point in CoSi, plotted along a $R - \Gamma - R$ trajectory. Colored dashed lines correspond to energy cuts in (b), which are fitted with a sum of Gaussian profiles on a linear background, by assuming a total of one and three peak(s) at and away from the Γ point, respectively, and under the constraint that equivalent **q** positions must have the same energies and peak widths. (c) and (d) Phonon intensities from INS experiment and the fitted-force-constant model, respectively, plotted along a $X - R - X$ trajectory near a charge-2 Dirac point in CoSi. (e) and (f) Similar to (c) and (d), but for MnSi and along an $M - R - M$ trajectory. (g) Energy cuts at a series of **Q** points using the same data as in (e) and (f). The INS and fitted model calculated data are displayed by circles and dashed lines, respectively. Open squares denote peak positions estimated from two-peak fits to the data (the fits are not shown), which form an approximate linear band crossing. Data in (b) and (g) are offset for clarity.

quite accurately accounts for the scattering cross sections, as seen from the colored dashed lines in Fig. 2(g), which actually represent model calculated intensities rather than peak fitting. This quantitative agreement suggests that it is possible to use the intensity information, from the experiment and/or the calculation, to elucidate the Chern number of a topological band crossing, which is our next subject.

IV. DETECTION OF CHERN NUMBERS BY NEUTRON SCATTERING

A. General theoretical scheme for twofold Weyl points

In this section, we will derive the explicit relation among phonon eigenvectors, Chern numbers, and the INS dynamical structure factor, using low-energy effective models near topological band crossing points. We will first present theoretical considerations for twofold Weyl points. Then, we will use the general formulism in our specific analyses of fourfold charge-2 Dirac points ($2\times$ twofold Weyl points) and quadruple Weyl points.

To begin with, for a twofold Weyl point, the effective Hamiltonian can be written as a 2×2 Hermitian matrix

$$H_{2\times2}(\mathbf{q}) = \sum_{i=x,y,z} f_i(\mathbf{q}) \cdot \sigma_i + f_0(\mathbf{q})\sigma_0, \quad (2)$$

where **q** is momentum measured from the Weyl point and σ_i are the Pauli matrices. In this notation, the eigenvector of one of the bands (e.g., the upper band) is represented by a spinor $\boldsymbol{\xi}^{\text{up}}(\mathbf{q}) = (\psi_1(\mathbf{q}), \psi_2(\mathbf{q}))^{\text{T}}$. We can further define a pseudospin quantity $\mathbf{S}(\mathbf{q})$ whose components are

$$S_i(\mathbf{q}) \equiv \frac{f_i(\mathbf{q})}{|\mathbf{f}(\mathbf{q})|} = \langle \xi^{\text{up}}|\sigma_i|\xi^{\text{up}}\rangle, \quad (3)$$

whose direction is represented by a point on the Bloch sphere $\mathbb{S}_{\text{B}}$. If we consider a surface $\mathbb{S}_{\mathbf{q}}$ enclosing the Weyl point in momentum space, on which a gap always exists between the upper and lower bands, a wrapping number can be used to characterize the mapping from $\mathbb{S}_{\mathbf{q}}$ to $\mathbb{S}_{\text{B}}$. This number is the Chern number $\pm C$ of the Weyl node [41], which does not depend on the shape of $\mathbb{S}_{\mathbf{q}}$. Specifically, $\mathbf{S}(\mathbf{q})$ will take every possible direction on $\mathbb{S}_{\text{B}}$ at least $|C|$ times as **q** moves around $\mathbb{S}_{\mathbf{q}}$. We will see examples of this in Figs. 3(b) and 4(a).

Next, we show that the pseudospin texture $\mathbf{S}(\mathbf{q})$ can leave distinct signatures in the INS dynamical structure factors. As we can see from Eq. (1), the dynamic structure factor $\mathcal{S}_{\text{coh}}^{(s)}(\mathbf{Q}, \omega)$ is sensitive to the inner product of $\boldsymbol{\xi}_d^{(s)}(\mathbf{q})$ and **Q**. Taking acoustic phonons for example, the INS intensity vanishes if the polarization vector $\boldsymbol{\xi}$ (same for all atoms for acoustic phonons) lies perpendicular to **Q**, and reaches maximum when the two vectors are parallel. For optical branches, similar conclusions are obtained by generalizing the real-space polarization vectors to abstract phonon eigenvectors in the Hilbert space. In the close vicinity of a Weyl node, assuming that $|\mathbf{Q}| \gg |\mathbf{q}|$ and $|\mathbf{q}| \ll 2\pi/a$, so that $\mathbf{Q} \approx \mathbf{G}$, the only fast varying term in the formula is the phonon eigenvector $\boldsymbol{\xi}^{\text{up}}(\mathbf{q})$. Using the pseudospin quantities, it is straightforward to show that the INS intensity of the upper band is approximately [44]

$$\mathcal{S}_{\text{coh}}^{\text{up}}(\mathbf{Q}, \omega) \propto |\mathbf{V}|(1 + \cos\langle\mathbf{S}(\mathbf{q}), \mathbf{V}(\mathbf{G})\rangle), \quad (4)$$

where $\mathbf{V}(\mathbf{G})$ is a constant vector that does not sensitively depend on **q** but varies between BZs, and $\langle\mathbf{S}, \mathbf{V}\rangle$ is the angle between two vectors. Both the pseudospin **S** and the vector **V** are vectors in the effective two-band Hilbert space, which ultimately represent certain lattice vibration modes. It then becomes clear that the INS intensity is related to a projection
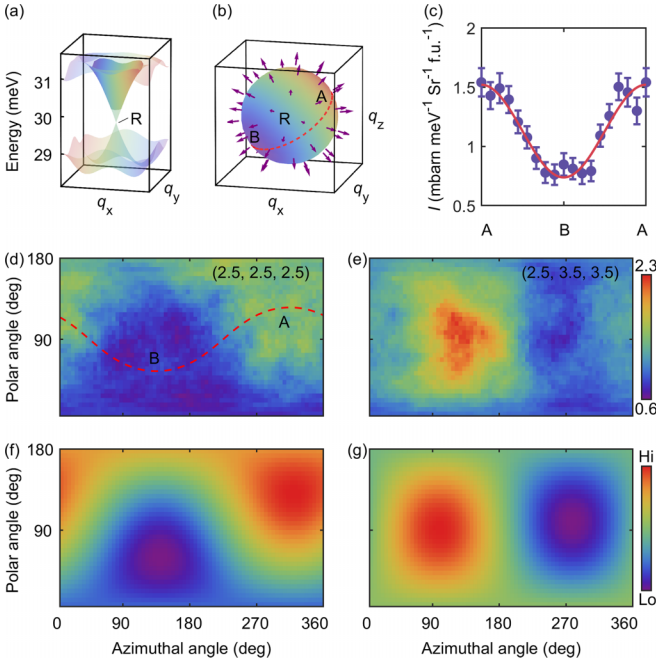
FIG. 3. (a) Phonon dispersions near the charge-2 Dirac point at 29.6 meV in MnSi. Solid color indicates energy integration range (30–32 meV). (b) Pseudospin texture on a **q** sphere enclosing the R point. Color indicates energy-integrated INS intensities near $\mathbf{Q} = (2.5, 2.5, 2.5)$. (c) INS intensity along the red circle $\widehat{ABA}$ in (b), fitted with a cosine function (red line, see text). (d) and (e) INS intensities averaged over solid **q** spheres enclosing (2.5, 2.5, 2.5) and (2.5, 3.5, 3.5) respectively, with a radius of 0.2 r.l.u. and a cone-smoothing width of $\pm 20°$. (e) and (f) Fitted-force-constant model calculations according to Eq. (4), for the same **q** spheres as in (d) and (e), respectively.

of $\mathbf{S}(\mathbf{q})$ along **V**. In particular, $\mathcal{S}_{\mathrm{coh}}^{\mathrm{up}}(\mathbf{Q}, \omega)$ would reach maximum when $\mathbf{S}(\mathbf{q})$ and **V** are parallel, and vanish when they are antiparallel.

Combining Eq. (4) with our former arguments about the wrapping (Chern) number, we come to the following explicit statement: On a momentum surface $\mathbb{S}_{\mathbf{q}}$ that encloses the Weyl node, there are at least $|C|$ momenta where pseudospin **S** is parallel to **V**, where the INS intensity of the upper band $\mathcal{S}_{\mathrm{coh}}^{\mathrm{up}}(\mathbf{Q}, \omega)$ reaches maximum. Similarly, there are also at least $|C|$ momenta where the intensity reaches zero. In most practical cases where the lowest-order $k \cdot p$ theory holds, the total numbers of maxima and zeros are simply $|C|$. The approximation of $\mathbf{Q} = \mathbf{q} + \mathbf{G} \approx \mathbf{G}$ can also be released since **Q** has trivial topology on the surface $\mathbb{S}_{\mathbf{q}}$ as long as the origin of **Q** is not enclosed. In summary, a Weyl node serves as a singular point of the pseudospin in momentum space, and the contrasting INS intensity distribution around it reveals its Chern number.

B. Charge-2 Dirac point

Now that we have linked the pseudospin texture with the INS intensity distribution, we next use it to analyze the charge-2 Dirac point in the phonon bands of MSi at the R point of the BZ. Although being fourfold degenerate, the effective
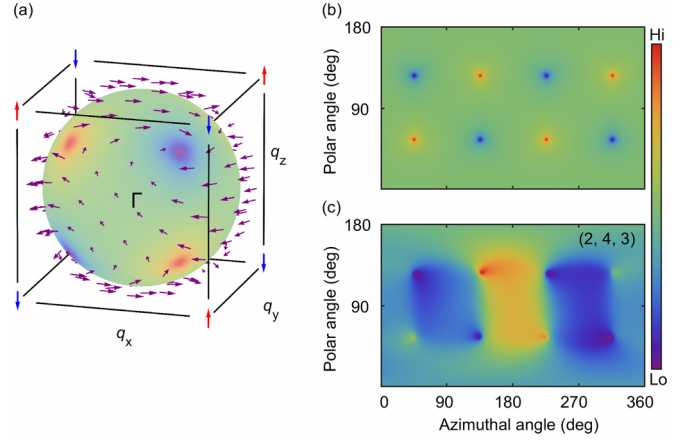

FIG. 4. (a) The pseudospin texture on a **q** sphere enclosing Γ, with the colors indicating the magnitude of S_z component. The orientations of **S** at eight diagonal directions are marked especially by blue and red arrows, showing tetrahedral symmetry. (b) S_z component of the pseudospin as a function of polar and azimuthal angles on the sphere. (c) Simulated INS intensity near $\mathbf{Q} = (2, 4, 3)$, showing similar patterns to (b) since **V** is almost in the z direction. All simulations are done with $|\mathbf{q}| = 0.05$ r.l.u. and for the upper band near the 40.1 meV band-crossing point in MnSi.

Hamiltonian near the band crossing $H_4(\mathbf{q}) \propto \begin{pmatrix} \mathbf{q} \cdot \sigma & 0 \\ 0 & \mathbf{q} \cdot \sigma \end{pmatrix}$ is the direct sum of that of two identical spin-1/2 Weyl points, each with Chern number $C = \pm 1$ [22]. The general relation between pseudospin and INS intensity can be easily generalized in this case with only minor modifications [44]. Namely, as long as the INS intensities of the two upper bands are considered as a whole, there will be exactly one maximum and one minimum on the enclosing $\mathbb{S}_{\mathbf{q}}$, i.e., resembling that of a regular spin-1/2 Weyl point. The only difference is an extra constant term in the intensity, so that the minimum is finite rather than zero [44].

For a concrete example, we inspect the INS intensities near a charge-2 Dirac point (at the BZ R point) at about 29.6 meV in MnSi. The phonon dispersion nearby is schematically shown in Fig. 3(a). On a small **q** sphere around the R point, the pseudospin texture is visualized in Fig. 3(b), where purple arrows indicate the pseudospin directions $\mathbf{S}(\mathbf{q})$. The outward hedgehog configuration of the arrows indicates that $\mathbf{S}(\mathbf{q})$ takes every direction once on the Bloch sphere, corresponding to Chern number $|C| = 1$.

From an experimental perspective, a **q** sphere as small as possible should be used to extract the INS intensity, in order to avoid an overlap with neighboring bands. But the sphere cannot be too small or thin, as otherwise the counting statistics would be too low. In our case, we find that binning INS data over a finite solid sphere produces satisfactory results, as the intensity modulations around topological nodes are robust and only weakly depends on the magnitude of $|\mathbf{q}|$ (Fig. S10 in [44]). In Fig. 3(d), intensities integrated over [30, 32] meV around $R = (2.5, 2.5, 2.5)$ are displayed as a function of the polar and azimuthal angles. The radius of the solid sphere is set to be 0.2 reciprocal lattice units (r.l.u.), and the displayed intensity at each angle represents the average over a cone volume within a $20°$ half-apex angle.

The above INS result agrees nicely with our fitted-force-constant model calculations [Fig. 3(f)]. To rationalize their characteristics with our effective model in Eq. (4), we note that due to the threefold rotational symmetry, the vector **V** for the Dirac point at $R = (2.5, 2.5, 2.5)$ is along the [111] direction. Consequently, the intensity will reach its maximum and minimum along the [111] and [$\bar{1}\bar{1}\bar{1}$] directions (or vice versa).

Moreover, on a great circle $\widehat{ABA}$ [red dashed lines in Figs. 3(b) and 3(d)] that passes through the [111] and [$\bar{1}\bar{1}\bar{1}$] directions, the intensity is expected to have a cosine dependence, which we also confirm experimentally [Fig. 3(c)].

Besides for the R point $(2.5, 2.5, 2.5)$ where the symmetry is high, the same analysis can be performed at other R points, such as $(2.5, 3.5, 3.5)$. The results [Figs. 3(e) and 3(g)] show that the extrema are no longer located along the diagonal direction, due to the different orientation of **V**. Nevertheless, the fact that the intensity exhibits one minimum and one maximum indicates that the underlying Chern number is $|C| = 1$.

C. Quadruple Weyl point

We further explore the quadruple Weyl points at the Γ point, which are protected by time-reversal symmetry $\mathcal{T} = K\sigma_x$ and have an unusual Chern number of ± 4. The effective phonon Hamiltonian near the band crossing point can be written as [41]

$$H_{2\times 2}(\mathbf{q}) = -\begin{pmatrix} Aq_x q_y q_z & B(q_x^2 + \omega q_y^2 + \omega^2 q_z^2) \\ B(q_x^2 + \omega^2 q_y^2 + \omega q_z^2) & -Aq_x q_y q_z \end{pmatrix},$$
(5)

where $\omega = \exp(-2\pi i/3)$, and A and B are real constants. We have omitted the kinetic energy term $f_0(\mathbf{q})$ that has nothing to do with the band topology. The pseudospin texture $\mathbf{S}(\mathbf{q})$ around the quadruple Weyl point is shown in Fig. 4(a). The S_z component of the pseudospin is illustrated by the colors on the spherical $\mathbf{q}$ surface in Fig. 4(a) and plotted on a flat map in Fig. 4(b). The direction of $\mathbf{S}(\mathbf{q})$ is almost always in the $q_x q_y$ plane except near [111] and equivalent diagonal directions. As indicated by the blue and red arrows in Fig. 4(a), the eight diagonal directions can be subdivided into two tetrahedron-vertex sets with opposite S_z, and the total wrapping number (Chern number) is $|C| = 4$.

An experimentally unfavorable aspect of the quadruple Weyl point is in the weak dispersion—the energy splitting between the two bands only increases as a quadratic (in most directions) or even a cubic (along [111] and its equivalents) function of **q**. This makes it difficult to separately measure $\mathcal{S}(\mathbf{Q}, \omega)$ of one of the bands. Moreover, all the quadruple Weyl points in MnSi and CoSi turn out to be close to other phonon branches. With the energy resolution of our INS experiment, it is not possible to extract the pseudospin texture of the quadruple Weyl points from the INS data. Nevertheless, our fitted-force-contants phonon model has no such resolution limits. In Fig. 4(c), we calculate $\mathcal{S}(\mathbf{Q}, \omega)$ of the upper band of the quadruple Weyl point at 40.1 meV in MnSi, on a 0.05 r.l.u. $|\mathbf{q}|$ sphere surrounding $\Gamma = (2, 4, 3)$. The BZ center $(2, 4, 3)$ is chosen because the **V** vector lies very close to the z direction, such that the INS intensities on the **q** sphere exhibit a similar distribution as the S_z component in Fig. 4(b), with

four maxima and four minima approximately along the $\langle 111 \rangle$ diagonal directions. This virtual measurement suggests that INS has in principle the capability to reveal the pseudospin's wrapping behavior (and hence the Chern number) associated with the novel quadruple Weyl points. It can be realized in experiments with higher resolution and/or in materials where the quadruple Weyl points are far away from other phonons.

V. DISCUSSION AND CONCLUSION

Our study demonstrates the capability of INS to measure Chern numbers of topological phonon band crossing. While scattering intensity varies with momentum even for nontopological bands, the unique spectroscopic characteristics of Weyl and Dirac points lie in the fact that they are singular points for eigenvectors, hence the intensity distribution around them exhibits abrupt variations: Even on an infinitely small enclosing momentum surface, the intensity modulations around the topological nodes are still present, whereas in the case of topologically trivial band crossings, the intensity distribution would approach a constant as the enclosing surface shrinks into a point. To provide a concrete example, simulated INS intensities around a trivial two-band crossing in MnSi are presented in Fig. S10 [44]. The intensity variations gradually disappear upon shrinking the **q** surface, in sharp contrast with the robust modulations around topological nodes. Consequently, in order to determine Chern numbers from INS experiments, it is better to study the close vicinity of the band crossing points, i.e., using a small **q** surface to both avoid other bands and ensure that the intensity modulations arise solely from the topology. We also note that the intensity modulations we discuss here are universal for twofold phonon Weyl points of any Chern number, as well as for some of the fourfold Dirac points. For other types of topological band crossings, e.g., the spin-1 Weyl points, similar abrupt intensity changes are also expected to occur because the Weyl points are still singularities of pseudospin texture, but it is unclear at this point whether our method for analyzing two-band crossing has useful multiband counterparts. According to group theory [56], phonon Weyl points exist in crystals of certain space groups, and they can be found at specific high-symmetry points in the BZ. As long as they are far away from other bands and have a relatively large group velocity, intensity modulations can be observable by INS.

The detection of wave functions (or, vibrational eigenvectors) is not restricted to INS experiments on phonons, and it can be a common capability of many spectroscopic methods. In polarization-dependent angle-resolved photoemission spectroscopy (ARPES), changes in the signal intensity have been suggested to reflect the wave functions of Dirac electrons [57]. Related measurements have also been proposed for resonant inelastic x-ray scattering (RIXS) [58]. While the wave-function texture of the quasiparticles is at the origin of all the spectroscopic observables, the specific interactions between the experimental probes and the quasiparticles may add further complexity to the interpretation of experiments. For instance, INS measurements of phonons involve neutron collisions with nuclei, giving rise to the $\mathbf{Q} \cdot \boldsymbol{\xi}$ term in the scattering cross section; and because **Q** uniquely determines **V** in Eq. (4), the associated projection of $\boldsymbol{\xi}$ always allows for

the determination of the Chern number. On the contrary, for magnon bands, dipole-dipole interactions between neutrons and magnetic moments lead to a $\mathbf{Q} \times (\mathbf{Q} \times \mathbf{S})$ term in the cross section, and the component of $\mathbf{S}$ parallel to $\mathbf{Q}$ is missing from the detection. As a result, the number of extrema in the intensity modulation on an enclosing momentum surface may change between different choices of the measurement BZ, rendering it necessary to have extra knowledge about the magnetic system in order to correctly infer the topological invariant. In the cases of ARPES and RIXS, complexity may arise because the different polarization channels have to be considered together. We note that the very same materials (MnSi and CoSi) could potentially be good model systems for such APRES measurements because they also possess multiple topological band crossings in their electronic bands with different Chern numbers [59–61]. To this end, our INS measurement of phonons may be regarded as a demonstration of principles that motivates further studies.

Lastly, we discuss the possibility of manipulating phonon band topology with external tuning. In MnSi and CoSi, the multiple Weyl points are protected by crystalline symmetries and are sensitive to symmetry-breaking external fields such as the strains. For example, a [111]-uniaxial strain breaks the quadruple Weyl point into four single Weyl points. However, it remains challenging to open a full gap between the two bands and to make the gap topological. The former is because a Weyl point can only be gapped by annihilation with another oppositely charged Weyl point, and the latter is because the topological classification is trivial for all bosonic gaps with the presence of time-reversal symmetry. Therefore, a topological phonon gap would require a density-wave order that folds the positive and negative Weyl points together, plus magnetism that couples to the phonons. Besides altering crystal structure (e.g., with strain), a practical approach is to break time-reversal symmetry with an external magnetic field or magnetic order. In such cases, degeneracies at some high-symmetric points might be lifted, e.g., the charge-2 Dirac points might split into two spin-1/2 Weyl points, and the quadruple Weyl points might split into two single bands. MnSi actually develops a spiral magnetic order below 29.5 K [62]. However, we do not observe any evident topological band splitting at $T = 4$ K (Fig. S9 [44]), possibly because the magnetoelastic coupling is too weak. Therefore, we conclude that studying symmetry-breaking effects on phonon band topology is hardly feasible in MnSi and CoSi, but the idea might be worthwhile to try in other materials.

In conclusion, we have performed a comprehensive study on the topological phonon band crossings in MnSi and CoSi. Both the band dispersions and the coherent dynamical structure factors are experimentally resolved with high precision, yielding results that compare well with model calculations. The existence of spin-1 Weyl points and charge-2 Dirac points in the phonon bands are verified by the measured dispersions. Combining experiments and model calculations, we further demonstrate the capability of INS for unambiguously determining Chern numbers of band crossing nodes. Our general theoretical scheme based on effective Hamiltonians suggests that related methods can be used in the study of other topological quasiparticles, as well as other spectroscopic methods.

[1] K. v. Klitzing, G. Dorda, and M. Pepper, New Method for High-Accuracy Determination of the Fine-Structure Constant Based on Quantized Hall Resistance, Phys. Rev. Lett. **45**, 494 (1980).

[2] D. J. Thouless, M. Kohmoto, M. P. Nightingale, and M. den Nijs, Quantized Hall Conductance in a Two-Dimensional Periodic Potential, Phys. Rev. Lett. **49**, 405 (1982).

[3] X.-L. Qi and S.-C. Zhang, Topological insulators and superconductors, Rev. Mod. Phys. **83**, 1057 (2011).

[4] A. A. Burkov, Topological semimetals, Nature Mater. **15**, 1145 (2016).

[5] A. Bansil, H. Lin, and T. Das, Colloquium: Topological band theory, Rev. Mod. Phys. **88**, 021004 (2016).

[6] C.-K. Chiu, J. C. Y. Teo, A. P. Schnyder, and S. Ryu, Classification of topological quantum matter with symmetries, Rev. Mod. Phys. **88**, 035005 (2016).

[7] N. P. Armitage, E. J. Mele, and A. Vishwanath, Weyl and Dirac semimetals in three-dimensional solids, Rev. Mod. Phys. **90**, 015001 (2018).

[8] A. Roth, C. Brüne, H. Buhmann, L. W. Molenkamp, J. Maciejko, X.-L. Qi, and S.-C. Zhang, Nonlocal transport in the quantum spin hall state, Science **325**, 294 (2009).

[9] X. Wan, A. M. Turner, A. Vishwanath, and S. Y. Savrasov, Topological semimetal and fermi-arc surface states in the electronic structure of pyrochlore iridates, Phys. Rev. B **83**, 205101 (2011).

[10] L. X. Yang, Z. K. Liu, Y. Sun, H. Peng, H. F. Yang, T. Zhang, B. Zhou, Y. Zhang, Y. F. Guo, M. Rahn, D. Prabhakaran, Z. Hussain, S.-K. Mo, C. Felser, B. Yan, and Y. L. Chen, Weyl semimetal phase in the non-centrosymmetric compound TaAs, Nature Phys. **11**, 728 (2015).

[11] B. Q. Lv, H. M. Weng, B. B. Fu, X. P. Wang, H. Miao, J. Ma, P. Richard, X. C. Huang, L. X. Zhao, G. F. Chen, Z. Fang, X. Dai, T. Qian, and H. Ding, Experimental Discovery of Weyl Semimetal TaAs, Phys. Rev. X **5**, 031013 (2015).

[12] F. de Juan, A. G. Grushin, T. Morimoto, and J. E. Moore, Quantized circular photogalvanic effect in Weyl semimetals, Nature Commun. **8**, 15995 (2017).

[13] F. Flicker, F. de Juan, B. Bradlyn, T. Morimoto, M. G. Vergniory, and A. G. Grushin, Chiral optical response of multi-fold fermions, Phys. Rev. B **98**, 155145 (2018).

[14] F. D. M. Haldane and S. Raghu, Possible Realization of Directional Optical Waveguides in Photonic Crystals with Broken Time-Reversal Symmetry, Phys. Rev. Lett. **100**, 013904 (2008).

[15] L. Lu, L. Fu, J. D. Joannopoulos, and M. Soljačić, Weyl points and line nodes in gyroid photonic crystals, Nature Photon. **7**, 294 (2013).

[16] L. Lu, Z. Wang, D. Ye, L. Ran, L. Fu, J. D. Joannopoulos, and M. Soljačić, Experimental observation of Weyl points, Science **349**, 622 (2015).

[17] M. Xiao, W.-J. Chen, W.-Y. He, and C. T. Chan, Synthetic gauge flux and Weyl points in acoustic systems, Nature Phys. **11**, 920 (2015).

[18] H. Ge, X. Ni, Y. Tian, S. K. Gupta, M.-H. Lu, X. Lin, W.-D. Huang, C. T. Chan, and Y.-F. Chen, Experimental Observation of Acoustic Weyl Points and Topological Surface States, Phys. Rev. Appl. **10**, 014017 (2018).

[19] S. A. Skirlo, L. Lu, Y. Igarashi, Q. Yan, J. Joannopoulos, and M. Soljačić, Experimental Observation of Large Chern Numbers in Photonic Crystals, Phys. Rev. Lett. **115**, 253901 (2015).

[20] H. He, C. Qiu, L. Ye, X. Cai, X. Fan, M. Ke, F. Zhang, and Z. Liu, Topological negative refraction of surface acoustic waves in a Weyl phononic crystal, Nature (London) **560**, 61 (2018).

[21] F. Li, X. Huang, J. Lu, J. Ma, and Z. Liu, Weyl points and fermi arcs in a chiral phononic crystal, Nature Phys. **14**, 30 (2018).

[22] T. Zhang, Z. Song, A. Alexandradinata, H. Weng, C. Fang, L. Lu, and Z. Fang, Double-Weyl Phonons in Transition-Metal Monosilicides, Phys. Rev. Lett. **120**, 016401 (2018).

[23] H. Miao, T. T. Zhang, L. Wang, D. Meyers, A. H. Said, Y. L. Wang, Y. G. Shi, H. M. Weng, Z. Fang, and M. P. M. Dean, Observation of Double Weyl Phonons in Parity-Breaking FeSi, Phys. Rev. Lett. **121**, 035302 (2018).

[24] J. Li, Q. Xie, S. Ullah, R. Li, H. Ma, D. Li, Y. Li, and X.-Q. Chen, Coexistent three-component and two-component Weyl phonons in TiS, ZrSe, and HfTe, Phys. Rev. B **97**, 054305 (2018).

[25] B. W. Xia, R. Wang, Z. J. Chen, Y. J. Zhao, and H. Xu, Symmetry-Protected Ideal Type-II Weyl Phonons in CdTe, Phys. Rev. Lett. **123**, 065501 (2019).

[26] H. Li, T. Zhang, A. Said, Y. Fu, G. Fabbris, D. G. Mazzone, J. Zhang, J. Lapano, H. N. Lee, H. C. Lei, M. P. M. Dean, S. Murakami, and H. Miao, Observation of a chiral wave function in the twofold-degenerate quadruple Weyl system BaPtGe, Phys. Rev. B **103**, 184301 (2021).

[27] F.-Y. Li, Y.-D. Li, Y. B. Kim, L. Balents, Y. Yu, and G. Chen, Weyl magnons in breathing pyrochlore antiferromagnets, Nature Commun. **7**, 12691 (2016).

[28] A. Mook, J. Henk, and I. Mertig, Tunable Magnon Weyl Points in Ferromagnetic Pyrochlores, Phys. Rev. Lett. **117**, 157204 (2016).

[29] K. Li, C. Li, J. Hu, Y. Li, and C. Fang, Dirac and Nodal Line Magnons in Three-Dimensional Antiferromagnets, Phys. Rev. Lett. **119**, 247202 (2017).

[30] W. Yao, C. Li, L. Wang, S. Xue, Y. Dan, K. Iida, K. Kamazawa, K. Li, C. Fang, and Y. Li, Topological spin excitations in a three-dimensional antiferromagnet, Nature Phys. **14**, 1011 (2018).

[31] S. Bao, J. Wang, W. Wang, Z. Cai, S. Li, Z. Ma, D. Wang, K. Ran, Z.-Y. Dong, D. L. Abernathy, S.-L. Yu, X. Wan, J.-X. Li, and J. Wen, Discovery of coexisting Dirac and triply degenerate magnons in a three-dimensional antiferromagnet, Nature Commun. **9**, 2591 (2018).

[32] L. Zhang, J. Ren, J.-S. Wang, and B. Li, Topological Nature of the Phonon Hall Effect, Phys. Rev. Lett. **105**, 225901 (2010).

[33] A. Mook, J. Henk, and I. Mertig, Magnon hall effect and topology in kagome lattices: A theoretical investigation, Phys. Rev. B **89**, 134409 (2014).

[34] J. P. Mathew, J. d. Pino, and E. Verhagen, Synthetic gauge fields for phonon transport in a nano-optomechanical system, Nature Nanotechnol. **15**, 198 (2020).

[35] S. W. Lovesey, *Theory of Neutron Scattering from Condensed Matter* (Oxford University Press, Oxford, 1984).

[36] G. L. Squires, *Introduction to the Theory of Thermal Neutron Scattering*, 3rd ed. (Cambridge University Press, Cambridge, 2012).

[37] S. Shivam, R. Coldea, R. Moessner, and P. McClarty, arXiv:1712.08535.

[38] M. Elliot, P. A. McClarty, D. Prabhakaran, R. D. Johnson, H. C. Walker, P. Manuel, and R. Coldea, Order-by-disorder from bond-dependent exchange and intensity signature of nodal quasiparticles in a honeycomb cobaltate, Nature Commun. **12**, 3936 (2021).

[39] A. Scheie, P. Laurell, P. A. McClarty, G. E. Granroth, M. B. Stone, R. Moessner, and S. E. Nagler, Spin-exchange hamiltonian and topological degeneracies in elemental gadolinium, Phys. Rev. B **105**, 104402 (2022).

[40] A. Scheie, P. Laurell, P. A. McClarty, G. E. Granroth, M. B. Stone, R. Moessner, and S. E. Nagler, Dirac Magnons, Nodal Lines, and Nodal Plane in Elemental Gadolinium, Phys. Rev. Lett. **128**, 097201 (2022).

[41] T. Zhang, R. Takahashi, C. Fang, and S. Murakami, Twofold quadruple Weyl nodes in chiral cubic crystals, Phys. Rev. B **102**, 125148 (2020).

[42] R. Kajimoto, M. Nakamura, Y. Inamura, F. Mizuno, K. Nakajima, S. Ohira-Kawamura, T. Yokoo, T. Nakatani, R. Maruyama, K. Soyama, K. Shibata, K. Suzuya, S. Sato, K. Aizawa, M. Arai, S. Wakimoto, M. Ishikado, S.-i. Shamoto, M. Fujita, H. Hiraka *et al.*, The Fermi Chopper Spectrometer 4SEASONS at J-PARC, J. Phys. Soc. Jpn. **80**, SB025 (2011).

[43] G. E. Granroth, A. I. Kolesnikov, T. E. Sherline, J. P. Clancy, K. A. Ross, J. P. C. Ruff, B. D. Gaulin, and S. E. Nagler, SEQUOIA: A newly operating chopper spectrometer at the SNS, J. Phys.: Conf. Ser. **251**, 012058 (2010).

[44] See Supplemental Material at http://link.aps.org/supplemental/10.1103/PhysRevB.106.224304 for additional measurement data and analysis.

[45] Z. Jin, Y. Li, Z. Hu, B. Hu, Y. Liu, K. Iida, K. Kamazawa, M. B. Stone, A. I. Kolesnikov, D. L. Abernathy, X. Zhang, H. Chen, Y. Wang, C. Fang, B. Wu, I. A. Zaliznyak, J. M. Tranquada, and Y. Li, arXiv:2206.13699.

[46] Y. Inamura, T. Nakatani, J. Suzuki, and T. Otomo, Development status of software "Utsusemi" for chopper spectrometers at MLF, J-PARC, J. Phys. Soc. Jpn. **82**, SA031 (2013).

[47] R. Ewings, A. Buts, M. Le, J. van Duijn, I. Bustinduy, and T. Perring, Horace: Software for the analysis of data from single crystal spectroscopy experiments at time-of-flight neutron instruments, Nucl. Instrum. Meth. Phys. Res. A **834**, 132 (2016).

[48] G. Xu, Z. Xu, and J. M. Tranquada, Absolute cross-section normalization of magnetic neutron scattering data, Rev. Sci. Instrum. **84**, 083906 (2013).

[49] X. Gonze and C. Lee, Dynamical matrices, born effective charges, dielectric permittivity tensors, and interatomic force constants from density-functional perturbation theory, Phys. Rev. B **55**, 10355 (1997).

[50] G. Kresse and J. Hafner, *Ab initio* molecular dynamics for liquid metals, Phys. Rev. B **47**, 558 (1993).

[51] G. Kresse and J. Hafner, Ab initio molecular-dynamics simulation of the liquid-metal–amorphous-semiconductor transition in germanium, Phys. Rev. B **49**, 14251 (1994).

[52] G. Kresse and J. Furthmüller, Efficiency of ab-initio total energy calculations for metals and semiconductors using a plane-wave basis set, Comput. Mater. Sci. **6**, 15 (1996).

[53] G. Kresse and J. Furthmüller, Efficient iterative schemes for ab initio total-energy calculations using a plane-wave basis set, Phys. Rev. B **54**, 11169 (1996).

[54] J. P. Perdew, K. Burke, and M. Ernzerhof, Generalized Gradient Approximation Made Simple, Phys. Rev. Lett. **77**, 3865 (1996).

[55] G. Shirane, S. M. Shapiro, and J. M. Tranquada, *Neutron Scattering with a Triple-Axis Spectrometer: Basic Techniques* (Cambridge University Press, Cambridge, 2002).

[56] Q.-B. Liu, Y. Qian, H.-H. Fu, and Z. Wang, Symmetry-enforced Weyl phonons, npj Comput. Mater. **6**, 95 (2020).

[57] C. Hwang, C.-H. Park, D. A. Siegel, A. V. Fedorov, S. G. Louie, and A. Lanzara, Direct measurement of quantum phases in graphene via photoemission spectroscopy, Phys. Rev. B **84**, 125422 (2011).

[58] S. Kourtis, Bulk spectroscopic measurement of the topological charge of Weyl nodes with resonant x rays, Phys. Rev. B **94**, 125132 (2016).

[59] P. Tang, Q. Zhou, and S.-C. Zhang, Multiple Types of Topological Fermions in Transition Metal Silicides, Phys. Rev. Lett. **119**, 206402 (2017).

[60] Z. Rao, H. Li, T. Zhang, S. Tian, C. Li, B. Fu, C. Tang, L. Wang, Z. Li, W. Fan, J. Li, Y. Huang, Z. Liu, Y. Long, C. Fang, H. Weng, Y. Shi, H. Lei, Y. Sun, T. Qian *et al.*, Observation of unconventional chiral fermions with long fermi arcs in CoSi, Nature (London) **567**, 496 (2019).

[61] M. A. Wilde, M. Dodenhöft, A. Niedermayr, A. Bauer, M. M. Hirschmann, K. Alpin, A. P. Schnyder, and C. Pfleiderer, Symmetry-enforced topological nodal planes at the fermi surface of a chiral magnet, Nature (London) **594**, 374 (2021).

[62] Y. Ishikawa, K. Tajima, D. Bloch, and M. Roth, Helical spin structure in manganese silicide MnSi, Solid State Commun. **19**, 525 (1976).